Physics of Plasmas

RESEARCH ARTICLE | JULY 07 2023

Wave analysis during energetic electron microinjections: A case study

K. Nykyri ; Y. Liou ; X. Ma; S. Kavosi ; J. Egedal ; S. A. Fuselier ; R. G Gomez

Phys. Plasmas 30, 072903 (2023)
https://doi.org/10.1063/5.0142938

AIP Publishing

Physics of Plasmas ARTICLE pubs.aip.org/aip/pop

Wave analysis during energetic electron microinjections: A case study

Cite as: Phys. Plasmas **30**, 072903 (2023); doi: 10.1063/5.0142938
Submitted: 18 January 2023 · Accepted: 9 June 2023 ·
Published Online: 7 July 2023

K. Nykyri,[1,a)] Y. Liou,[1] X. Ma,[1] S. Kavosi,[1] J. Egedal,[2] S. A. Fuselier,[3,4] and R. G Gomez[3]

AFFILIATIONS

[1]Department of Physical Sciences and Center for Space and Atmospheric Research, Embry-Riddle Aeronautical University, Daytona Beach, Florida 32114, USA
[2]Physics Department, University of Wisconsin Madison, Madison, Wisconsin 53706, USA
[3]Southwest Research Institute, San Antonio, Texas 78238, USA
[4]University of Texas at San Antonio, San Antonio, Texas 78249, USA

[a)]**Author to whom correspondence should be addressed:** nykyrik@erau.edu

ABSTRACT

The Magnetospheric Multi-scale Mission has frequently observed periodic bursts of counterstreaming electrons with energies ranging from ≈30 to 500 keV at the Earth's magnetospheric boundary layers, termed "microinjections." Recently, a source region for microinjections was discovered at the high-latitude magnetosphere where microinjections showed up simultaneously at all energy channels and were organized by magnetic field variation associated with ultra low frequency mirror mode waves (MMWs) with ≈5 min periodicity. These MMWs were associated with strong higher frequency electromagnetic wave activity. Here, we have identified some of these waves as electromagnetic ion cyclotron (EMIC) waves. EMIC waves and parallel electric fields often lead to the radiation belt electron losses due to pitch-angle scattering. We show that, for the present event, the EMIC waves are not responsible for scattering electrons into a loss cone, and thus, they are unlikely to be responsible for the observed microinjection signature. We also find that the parallel electric field potentials within the waves are not adequate to explain the observed electrons with >90 keV energies. While whistler waves may contribute to the electron scattering and may exist during this event, there was no burst mode data available to verify this.

I. INTRODUCTION

Relativistic electrons with MeV energies in the Earth's radiation belts require a seed population of tens to hundreds of keV energies. Magnetic reconnection in the Earth's magnetotail during substorms has been considered as one of the main mechanisms generating this seed population,[1] where the particles energized by the reconnection process are injected into the inner magnetosphere.[2] "Microinjections" are more localized than traditional injections and have been observed both at dawn and dusk sectors of the plasma sheet.[3,4] As the gradient-curvature drift is energy-dependent with higher energies drifting faster, spacecraft outside of the source region observe an energy-dispersed signature.[4]

Kelvin–Helmholtz waves and flux transfer events at the dusk flank magnetopause have been proposed as possible candidate mechanisms generating microinjections,[5] which were observed by the magnetospheric multi-scale (MMS) further away from their source region.[4] Recently, MMS spacecraft traversed through the potential source region of the microinjections at the dusk sector, dayside, high-latitude boundary layer. Counterstreaming, high-energy electrons (≈29–550 keV) were simultaneously observed both at low and high-energies, thus lacking the dispersion signature. The counterstreaming electron fluxes were localized in the troughs of mirror mode waves (MMWs). It was suggested that the local energization mechanisms[6] in nearby diamagnetic cavities (DMCs)[7] were responsible for the ion temperature anisotropy within magnetosphere enabling drift mirror instability and growth of mirror mode waves in their peak mode.[8]

As the DMCs contain an abundance of tens to hundreds of keV energy electrons and can form in the vicinity of the high-altitude cusps for any interplanetary magnetic field (IMF) orientation,[7–10] it has been suggested that they may form a dayside source for the seed population of the radiation belt electrons.[8] However, the detailed physical mechanisms of how these trapped electrons from DMCs may escape to the inner magnetosphere have remained unknown.

There is an abundance of studies that show how electromagnetic ion cyclotron (EMIC) waves, which are generated by the cyclotron instability of anisotropic ion distributions, lead to pitch-angle scattering of high-energy electrons into the Earth's atmosphere.[11–13] However, how

the MMWs cause the pitch-angle scattering of high-energy electrons is still unknown. Here, we investigate the EMIC wave and electric field properties within MMWs to better understand and eliminate physical mechanisms that scatter the locally trapped electrons with ≈30°–120° pitch angle distributions (PADs), as observed in the DMCs,[7,8,10] into the local loss cone exhibiting the counterstreaming PADs.

II. METHODOLOGY

A. Spacecraft data and instruments

This study uses level 2 data from NASA's MMS satellites.[14] Fast plasma investigation (FPI)[15] provides lower energy ion and electron energy spectra, moments, and electron velocity distribution functions. The flux gate magnetometers (FGMs)[16,17] provide the magnetic field. The hot plasma composition analyzer (HPCA) provides the H+ and O+ ion moments, O+ phase space-energy spectrograms, and velocity distribution functions.[18] Energetic electron and pitch angle (PA) distributions are recorded by Fly's eye energetic particle spectrometer (FEEPS)[19] instrument and from energetic particle detector (EPD).[20] The electric field is from spin-plane, and axial double probes (EDPs).[17,21,22] Solar wind conditions in Fig. 1(j) are from the OMNI (http://omniweb.gsfc.nasa.gov/) database.[23]

B. Waves in homogeneous, anisotropic, and multicomponent plasmas (WHAMP)-analysis

The WHAMP dispersion solver[24] is applied for the study of excitation and damping of plasma wave modes during an MMS wave event between 17:24:00 and 17:27:30 UT. As inputs to this solver, we use the observed H+, O+, and electron velocity distribution functions between 17:26:18 and 17:26:48 UT. These waves and particle distributions show variations due to wave-particle interactions but are quite representative of the microinjection event as a whole. The He+ and He++ concentrations were much smaller than O+ and were, thus, ignored in this study. The WHAMP distribution for each particle species is constructed by superposing three velocity distribution functions of that species normalized to the appropriate density factor to resemble the observed MMS distribution at that time. When searching for a solution [real and imaginary parts of the wave frequency as a function of the parallel ($k_\parallel$) and perpendicular ($k_\perp$) wave number], the input wave vectors and frequencies for this nine-component plasma model are initially normalized with respect to H+ such that $k_\perp^1 = k_\perp V_{th}^1/\Omega^1$, $k_\parallel^1 = k_\parallel V_{th}^1/\Omega^1$, and $f^1 = f/\Omega^1$. Here, Ω^1 is the proton gyro frequency in Hz ($\Omega^1 = eB/(2\pi m_p)$). The thermal speed for protons is $V_{th}^1 = \sqrt{2k_b T_{H+}/m_{H+}}$, where k_b is the Boltzmann constant, m_{H+} is the proton mass, B is the magnetic field strength, and T_{H+} is the proton temperature in Kelvins. Using the following observed plasma parameter values during the wave observations, $T_{H+} = 5300$ eV $= 61.42$ MK, $B = 36$ nT, gives $V_{Th}^1 = 1008$ km/s and $\Omega^1 = 0.5489$ Hz. The thermal proton gyroradius is $r_p = V_{Th}^1/2\pi\Omega^1 = 290$ km. See the data availability section for further details and the link to the WHAMP input.

III. RESULTS

A. Event overview

Figure 1 shows a summary of 11 h of MMS observations on October 2, 2015 between 8:00 and 19:00 UT with panel (a) showing

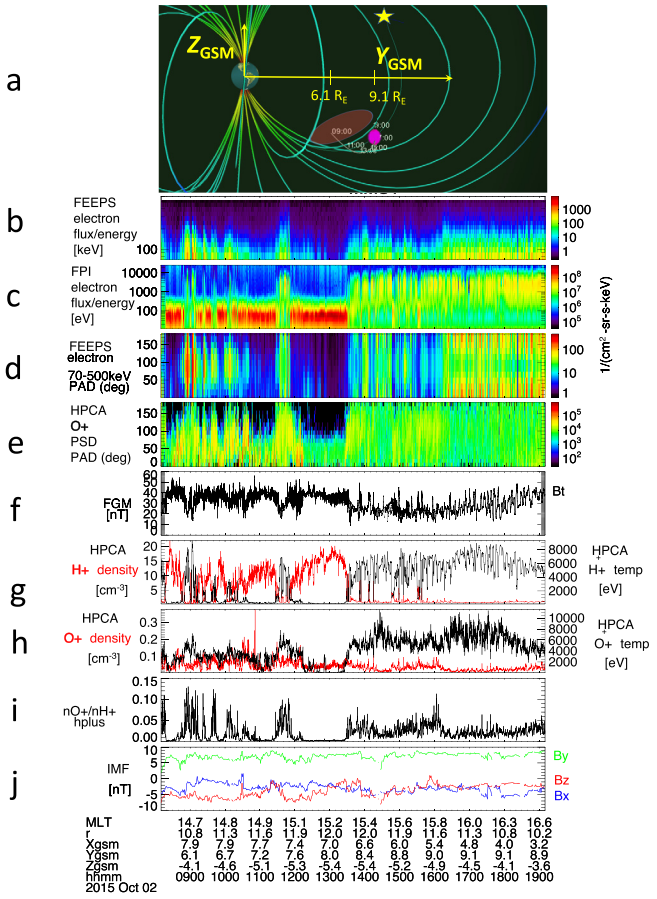

FIG. 1. Summary of the MMS observations on October 2, 2015 at 9:00–19:00 UT. (a) MMS orbit in dayside magnetosphere with Earth's magnetic field visualized with Tsyganenko 96-model. Oval depicts approximate diamagnetic cavity location as determined from observations and simulations.[7,8] (b) and (c) FEEPS and FPI electron spectrograms. (d) 70–500 keV energetic electron pitch angle distributions (PADs) from FEEPS. (e) O+ PADs from HPCA, (f) magnetic field strength, (g) and (h) H+ and O+ densities (red line) and temperatures (black line), respectively, (i) O+ to H+ number density ratio. (j) Interplanetary magnetic field (IMF) components. Panel (a) is reproduced from corresponding author's previous article.[8] Reproduced with permission from Nykyri *et al.*, Geophys. Res. Lett. **48**, 9 (2021). Copyright 2021 American Geophysical Union.

the MMS orbit and the location of the DMC created by low-latitude reconnection at 8:50–9:25 UT.[7] The energetic electron fluxes, as observed by FEEPS (b) and FPI (c), are enhanced in the DMCs, which are characterized by strongly perpendicular electron pitch angle distributions (PADs) at high energies (70–500 keV) (d). The cavity intervals are characterized by the weak magnetic field (f) and coincide with enhanced H+ (g) and O+ (h) temperatures. The origin of the O+ is likely the ionospheric outflow that gets trapped in the cavity by a strong mirror force at both edges of the cavity, one at the ionospheric and other at the magnetosheath-side.[7] On the high-latitude, magnetosheath side, the strong magnetic field gradient, which produces the second mirror point, is created by the kink in the reconnected and accumulated magnetic flux.[7] The formation of this second mirror point is unique to this topology and enabled by the 3D, curved field

line geometry in the vicinity of the high-altitude, exterior cusp. The O+ to H+ density ratio is enhanced in the cavities, because they are closer to the O+ source region (the ionosphere). After the quasi-periodic DMC encounters until 10:50 UT, MMS moves into a higher negative z-coordinate and encounters two magnetosheath intervals that are associated with boundary location change due to satellite position and IMF B_z change. The magnetosheath is characterized by higher H+ number density, lower plasma temperature, and lack of energetic electrons and O+ ions. After 13:30 UT, MMS enters a high-latitude boundary layer with strong fluctuations in magnetic field strength, B_t. The first set of B_t fluctuations shows both isotropic, closely perpendicular, and counterstreaming PADs, but between 16:00 and 19:00 they become more organized with strong enhancements in parallel and anti-parallel (with respect to the magnetic field) directions. These magnetic field fluctuations satisfy the drift mirror instability criteria, which generate mirror mode waves in their peak modes such that the trough regions are associated with the counterstreaming high-energy electrons [see, e.g., 17:27–17:30 UT in Fig. 2(a)]. These are visible at multiple FEEPS and EPD energy channels,[8] suggesting that MMS is at the source region of the microinjections. Such a counterstreaming signature could be observed in the spacecraft frame if the spacecraft is located between two reflection points. The counterstreaming electron fluxes drop during enhanced magnetic field regions [see, e.g., 17:25–17:26 UT in Fig. 2(a)].

Next, we address whether the origin and loss of these counterstreaming energetic electrons are related through scattering due to the ion frequency scale wave dynamics within the MMWs.

B. Wave observations

Figure 2 shows MMS wave and energetic particle observations between 17:20 and 17:50 UT (see caption for more details). Counterstreaming electrons (a) are enhanced in the magnetic field (b) depressions, while the fluxes are reduced and more isotropic in high-field regions. Electric fields (c) and (d) and fluctuations are enhanced at the gradients and voids of the electron fluxes where the magnetic field is typically high. Maximum magnetic field fluctuations (e) typically coincide with the maximum electric field fluctuations except for intervals close to 17:30 UT. The wave spectrum is mostly electromagnetic (f) as the $dE/(dBV_A)$ ratio is of the order of unity in the vicinity of ion frequencies but becomes more electrostatic at higher frequencies. Well-defined ($\lambda_M/\lambda_N > 100$) left-handed (in spacecraft frame) waves propagating at oblique angles (50°–55°) are observed at the vicinity of local oxygen cyclotron frequency (at 0.034 Hz) indicated by a vertical bar (g) suggesting these may be oxygen cyclotron waves. Another group, with well-defined eigenvalue ratios, of left-hand polarized, more parallel (5°–15°) propagating waves are detected at the vicinity of local proton cyclotron frequency at 0.55 Hz, which could be proton cyclotron waves.

C. WHAMP analysis of plasma wave growth

To study the plasma wave growth and damping, we have analyzed MMS ion and electron velocity distribution functions between 17:24 and 17:27:30 UT. Panels in Figs. 3(a)–3(c) show the observed H+, O+, and electron velocity distribution functions, respectively, in

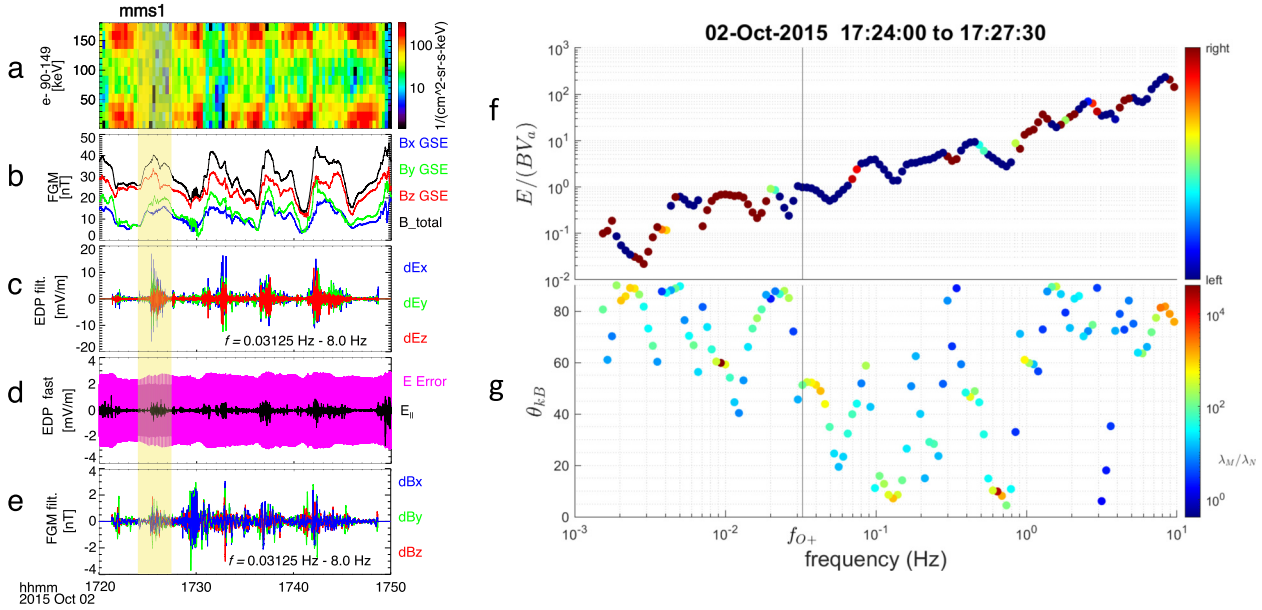

FIG. 2. Plasma wave observations during microinjections. (a) PADS of 90–149 keV electrons. (b) Magnetic field. (c) Electric field components bandpass filtered between 0.03125 and 8.0 Hz. (d) Parallel electric field and error in the total electric field. (e) Magnetic field components bandpass filtered between 0.03125 and 8.0 Hz. (f) Wave electric- to magnetic-field ratio normalized to local Alfvén speed, V_a ($E/(BV_a) = \frac{\sum E_\perp^2}{\sum B_\perp^2 V_A}$) and wave polarization (color code), as a function of the frequency computed using wavelet analysis of the non-filtered electric and magnetic fields between 17:24 and 17:27:30 UT (corresponding to the yellow highlighted column in left figure). The perpendicular electric and magnetic field fluctuations at each frequency are computed from maximum and intermediate components using minimum variance analysis. (g) Wave propagation angle and intermediate to minimum eigenvalue ratio (color code) as a function of frequency. Panels (a)–(e) are reproduced from supplementary material file shown in corresponding author's previous article.[8] Reproduced with permission from Nykyri *et al.*, Geophys. Res. Lett. **48**, 9 (2021). Copyright 2021 American Geophysical Union.

the spacecraft frame. (Bulk velocity is highly variable but typically less than 1/10th of the proton thermal speed.[8]) Panels in Figs. 3(d)–3(f) show the numerical distributions, each created by combining three different distributions (in order to mimic the observed distributions) with different temperature asymmetries and with density factor normalized to HPCA and FPI calculated number densities for ions and electrons, respectively. The H+ distribution is characterized by a shell with slight temperature asymmetry of $T_\perp/T_\parallel = 9/10$ at low energies and temperature asymmetry of $T_\perp/T_\parallel = 7/4$ at high energies. The O+ ions show a shell distribution at energies of ≈2–18 keV and two colder distributions. The electrons show symmetric Maxwellian at low energies, cigar-like distribution ($T_\perp/T_\parallel = 3/8$) at intermediate energies, and slightly asymmetric ($T_\perp/T_\parallel = 11/10$) at higher energies.

Figure 4 shows the solution of the WHAMP dispersion surface for imaginary (a) and (c) and real frequency (b) and (d) normalized to oxygen cyclotron frequency. The ellipticity (a) and (b) and the *dE*/*dB*-ratio (c) and (d) are color coded. Panels show the existence of electromagnetic (c) and (d) obliquely propagating, left-handed waves below the oxygen cyclotron frequency (b) that are effectively damped ($-\gamma/f > 10\%$) likely due to the presence of cold O+-ions (a).

Figure 5 is driven with the same plasma model and is in the same format as Fig. 4 but now showing solutions above the oxygen cyclotron frequency and below the proton cyclotron frequency. These waves are usually called proton-band EMIC waves. Waves are all left-handed (ellipticity < 0) and mostly electromagnetic ($E/B \approx V_A$). The maximum wave growth ($\gamma = 0.0017$) occurs for $\omega = 0.4155$ and for $k_\parallel^1 = 0.3090$, which corresponds to $k_\parallel = 1.68 \times e^{-7}/$ m. The wave propagation angles with respect to magnetic field, $\theta_{kB} = \tan^{-1}(k_\perp^1/k_\parallel^1)$, vary from 0.5° to 13° and $E/B \approx 1.5 V_A$ for a range of $k_\parallel^1$ and $k_\perp^1$ in the vicinity of the maximum wave growth [red region in Fig. 5(a)]. These angles and *E*/*B*-ratios are in reasonable agreement with the observed waves below the proton cyclotron frequency shown in Figs. 2(f) and 2(g). We find the same dispersion surfaces by varying the magnetic field between 28 and 38 nT and slightly adjusting the temperature asymmetries. Note that all the solutions shown in Figs. 4 and 5 show a non-zero real frequency, such that these waves with $0.4 f_{O+} < f < f_{H+}$ are not mirror mode waves (which are non-propagating and have nearly zero real frequency). These results suggest that the left handed waves observed by MMS below the proton cyclotron frequency and the observed velocity distributions during 17:24:00–17:27:30 UT can drive EMIC wave activity, but the oxygen cyclotron waves are more strongly damped than the proton cyclotron waves. For this event, the spacecraft separations of ≈20–30 km were too small, compared to wavelengths, to use

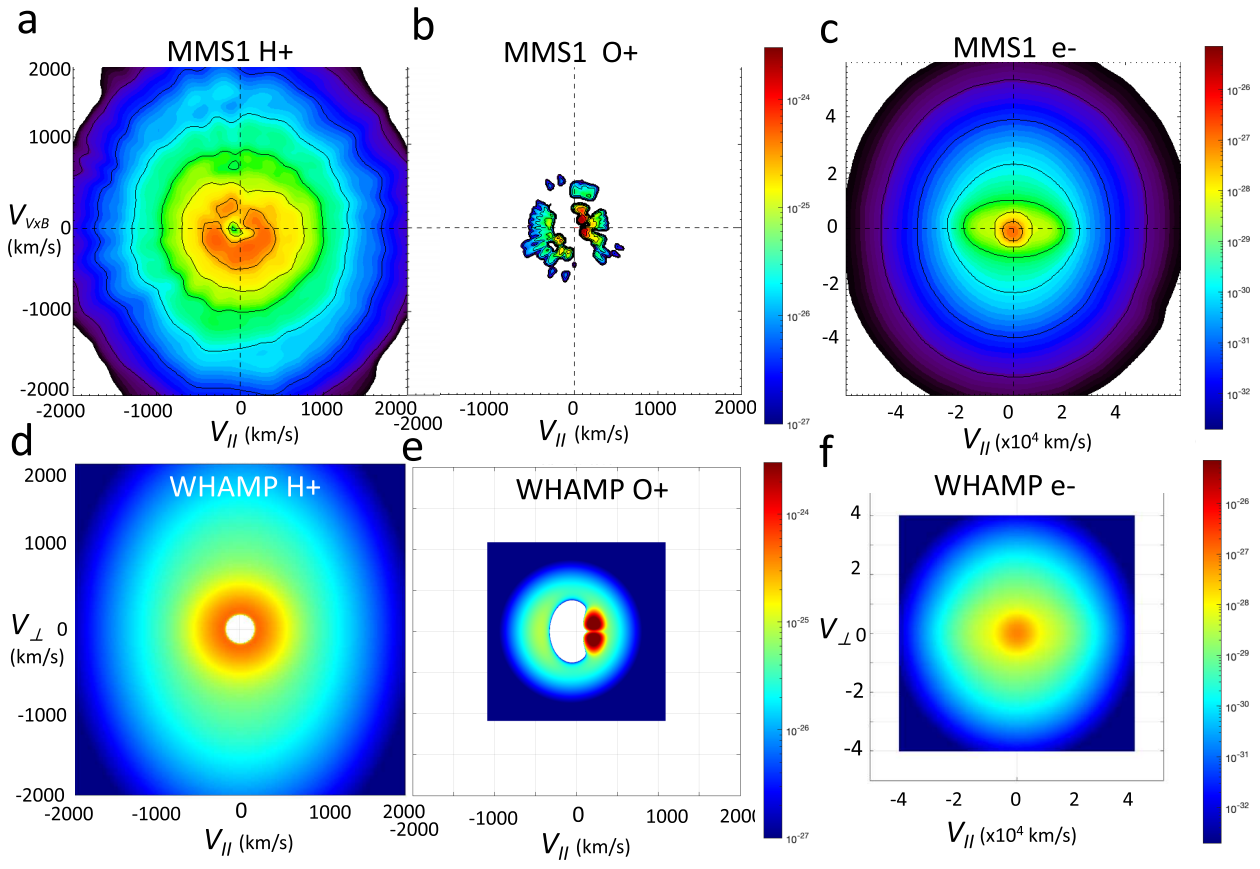

FIG. 3. The H+ (a) and O+ (b) velocity distributions observed between 17:26:28 and 17:26:48 UT in parallel ($V_\parallel$) and perpendicular ($V_V \times \mathbf{B}$)-planes. The same for the electrons is shown for 17:26:18–17:26:41 UT (c). Panels (d)–(f) show the corresponding artificially constructed velocity distributions used as an input to the WHAMP model.

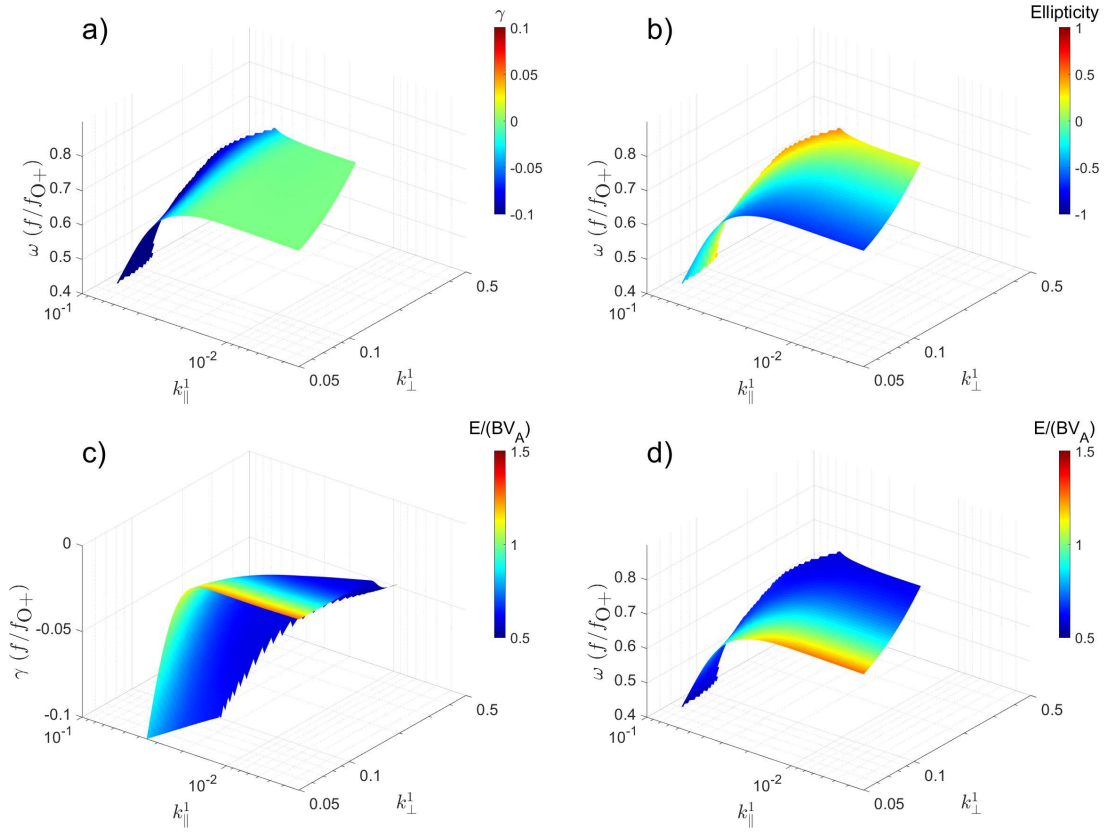

FIG. 4. Dispersion surfaces created for input shown in Fig. 3: Panels (a) and (b) show the real parts, ω, of the wave frequency normalized to the oxygen cyclotron frequency as a function of parallel ($k_\parallel$) and perpendicular ($k_\perp$) wave vectors that are normalized to ratio of proton thermal speed and proton gyro-frequency, v_{th}^1/Ω_1. The color code shows the wave growth rate, γ (a), and ellipticity (b). Panels (c) and (d) show the γ (ω) as a function of wavenumbers but now the color code is the wave electric field to magnetic field ratio normalized to the Alfvén speed, $E/(BV_A)$.

multi-spacecraft techniques[25,26] for experimental wave mode identification at the ion frequency range.

D. Resonance condition for energetic electrons

The relativistic Doppler condition for gyroresonance between electrons with an angular frequency of Ω_e and electromagnetic waves of angular frequency, ω, and parallel wave number, $k_\parallel$ may be written[27] as

$$\omega - k_\parallel v_\parallel = \varepsilon|\Omega_e|/\gamma, \tag{1}$$

where $\gamma = (1 - v^2/c^2)^{-1/2}$ is the Lorentz factor, the $v^2 = v_\parallel^2 + v_\perp^2$ is the square of the electron speed, and c is the speed of light. For resonance with left-hand polarized electromagnetic ion cyclotron (EMIC) waves, the factor ε has a negative integer value of -1.

The resonance condition then becomes

$$\omega - k_\parallel v_\parallel = -|\Omega_e|\sqrt{1 - \frac{(v_\parallel^2 + v_\perp^2)}{c^2}}, \tag{2}$$

which can also be expressed in terms of the particle's speed and pitch angle, α as

$$\omega - k_\parallel v \cos(\alpha) = -|\Omega_e|\sqrt{1 - \frac{v^2}{c^2}}, \tag{3}$$

where m_e is the electron mass, and this equation can be solved numerically as a function of v and α and by taking the values for ω, $k_\parallel$ from the WHAMP solution of the proton cyclotron waves, and computing $\Omega_e = eB/m_e$ using the B input value to WHAMP.

Figure 6 shows the left- and right-hand sides of Eq. (3) as a function of the electron velocity, which is computed from relativistic momentum for particle energies from 50 keV to 6 MeV for electron pitch angles of 0°, 30°, or 60°. Taking $\omega = -2\pi\,0.4155\,\Omega_{H+}$, which corresponds to the maximum wave growth ($\gamma = 0.0017$) at $k_\parallel = 1.68 \times e^{-7}/\mathrm{m}$, shows that the lines do not cross at energies even up to 6 MeV. This demonstrates that the electrons with the observed energies below 500 keV cannot be in resonance with the proton cyclotron waves with these properties.

E. Parallel potential associated with parallel electric field

Figures 2(c) and 2(d) also show that the dynamics contain electric field fluctuations up to ≈20–30 mV/m and modest parallel electric fields of the order of 1–2 mV/m. Parallel electric fields are

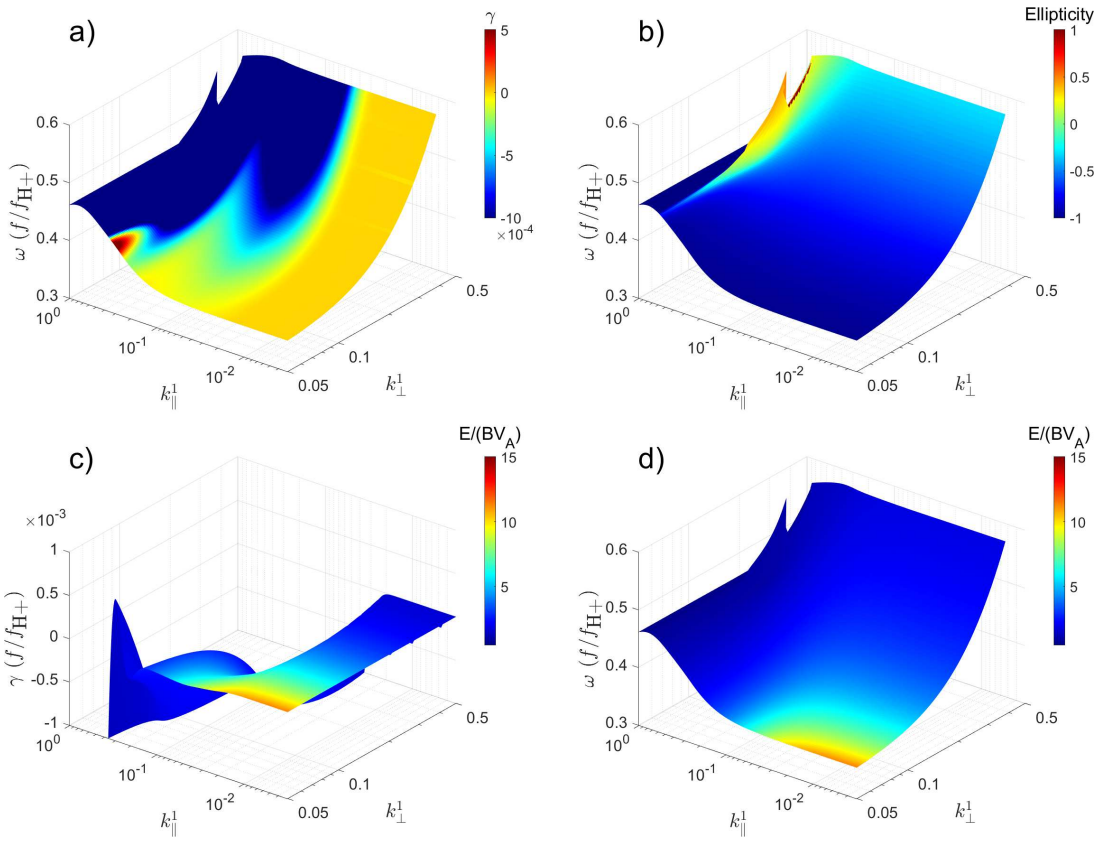

FIG. 5. Figure uses the same plasma model and is in the same format as Fig. 4 but now presenting WHAMP solutions for waves below the proton cyclotron frequency, f_{H+}.

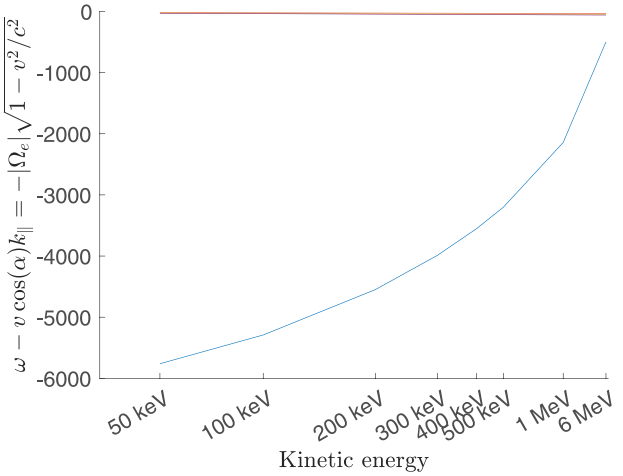

FIG. 6. The left (the straight lines) and right-hand (blue curved line) sides of Eq. (3) plotted as a function of electron kinetic energy, *KE*, for pitch angles, $\alpha = 60^\circ$ (yellow), 30° (orange), and 0° (blue). These kinetic energies correspond to speeds of $[1.24, 1.64, 2.08, 2.33, 2.48, 2.59, 2.82, 2.99]\ 1 \times 10^8$ m/s, respectively. The different pitch-angle curves appear overlapping when using this *y*-axis scale. Nevertheless, the key point is that they do not intersect with the right-hand side of Eq. (3).

characteristics for several plasma wave modes, e.g., kinetic Alfvén waves and whistler waves.[26] We next investigate whether these parallel electric fields are important for the observed microinjection signatures.

The distribution functions displayed in Figs. 7(a)–7(c) are calculated based on the full 3D electron data recorded by the fast plasma investigation[15] onboard MMS1, corresponding to the times marked by the dashed lines in Figs. 7(d) and 7(e). Furthermore, the distribution in Fig. 7(b) presents the same data as displayed in Fig. 3(c), and Figs. 7(d) and 7(e) cover the same time interval as Fig. 2.

Electrons streaming parallel and anti-parallel to the magnetic field are particularly sensitive to the effects of $E_{||}$, and the integrated effect of $E_{||}$ yields signatures in $f_e(\mathbf{v})$ from which the parallel potential $\Phi_{||} = \int_{\mathbf{x}}^{\infty} E_{||} dl$ can be inferred.[28–30] Here, the integral is computed from a given point $\mathbf{x}$ along the magnetic field out to the ambient plasma sourcing the passing electrons streaming mostly parallel to the magnetic field lines.

The distribution in Fig. 7(c) is very similar in its anisotropic feature to that observed by Wind and analyzed in Ref. 28. For example, the red line here shows $f_e(\mathscr{E}, \theta)$ for $\mathscr{E} = 1024$ eV as a function of the pitch angle $\theta = \arccos(\mathbf{v} \cdot \mathbf{B}/|\mathbf{v}||\mathbf{b}|)$, and it is observed how f_e is enhanced at $\theta \simeq 0^\circ$ and $\theta \simeq 180^\circ$. This is evidence that $e\Phi_{||} \simeq 1$ keV at this location.

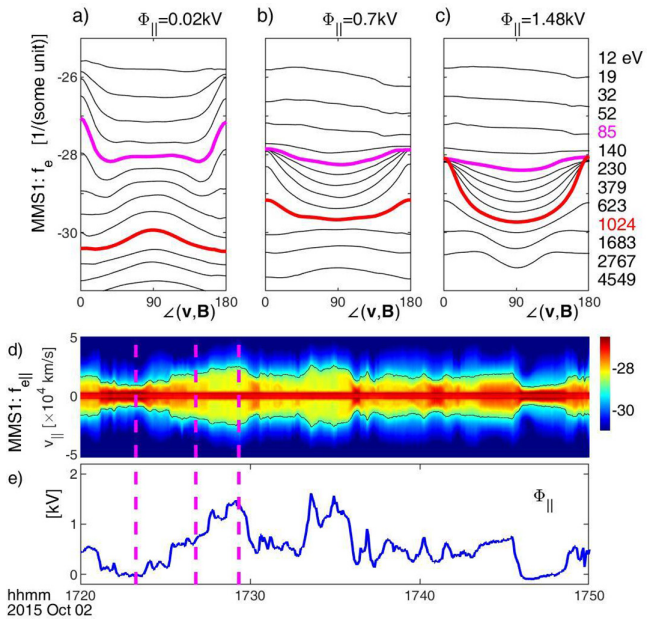

FIG. 7. (a)–(c) MMS1 FPI electron distributions were measured at times indicated in (d) and (e). Each line corresponds to a particular energy listed on the right, and the lines show f_e as a function of the pitch angle $\theta = \angle(\mathbf{v}, \mathbf{B})$. (d) Measured parallel distribution, $f_e(v_{||}, v_\perp = 0)$ shown as a function of time. From the black contours corresponding to $f_e(v_{||}, v_\perp = 0) = 10^{-29}\mathrm{s}^3/\mathrm{cm}^6$, the parallel potential, $\Phi_{||}$ in (e) is inferred.

Using a drift-kinetic framework,[29] the parallel and anti-parallel streaming electrons have $f(\mathscr{E}_{||}, \mathscr{E}_\perp \simeq 0) \simeq f_\infty(\mathscr{E}_{||}, e\Phi_{||})$, where $f_\infty(\mathscr{E})$ represents an assumed isotropic electron distribution of the ambient plasma sourcing the incoming electrons. By the methods developed in Ref. 30, this observation can be applied for estimating $\Phi_{||}$. In Fig. 7(d), we display $f_e(v_{||}, v_\perp \simeq 0)$ as a function of time. Using the black contour corresponding to $f_e(v_{||}, v_\perp \simeq 0) = 10^{-29}\mathrm{s}^3/\mathrm{cm}^6$, the potential profile in Fig. 7(e) is obtained. While $\Phi_{||}$ does include oscillations correlated with the microinjections, it is generally observed that $\Phi_{||} < 2$ keV. We, therefore, conclude that the parallel electric fields observed at these lower frequencies are simply not sufficiently strong to explain the acceleration of the >90 keV microinjected electrons. However, whistler waves may contribute to scattering, and future work should study existence of high-frequency whistler waves and resonance with the observed 50–500 keV electrons. For the present event, there is no burst mode magnetic field data available to study the possible existence of high frequency whistler waves.

IV. CONCLUSIONS AND DISCUSSION

In this study, we have analyzed plasma wave field properties close to ion frequencies, particle velocity distribution functions, and phase space densities as measured by MMS spacecraft to understand whether the EMIC waves or parallel electric fields within MMWs could be responsible for scattering energetic electrons into the loss cone and, thus, form the counterstreaming "microinjection"-signature. The free energy for EMIC wave generation mostly originates from the temperature anisotropy of the H+ ions in high beta plasma [see Fig. 4(j) in Ref. 26 and velocity distribution of hot-component H+ in Fig. 3]. The results are summarized as follows:

1. We identify the low-frequency, obliquely propagating, and closely parallel propagating left-handed waves as oxygen and proton cyclotron waves, respectively. The WHAMP solution shows positive wave growth for proton cyclotron waves, but their parallel wave number for all electron pitch angles is too small to allow resonance with electrons with energies from 50 to 500 keV. Thus, it is unlikely that these EMIC waves are responsible for scattering the electrons into the loss cone.
2. The parallel electrostatic potential during microinjections was inferred to be less than 2 keV and, thus, likely not important for the dynamics of the tens to hundreds of keV electrons.

These results suggest that the EMIC waves, associated cyclotron resonances, and parallel electric fields within MMWs are not responsible for the microinjection signature, at least for the present event.

Our future work will focus on testing other theories such as (i) possible existence and resonance with electron whistler waves and (ii) magnetic pumping[31,32] in drift mirror instability and associated MMW activity and simultaneous leakage of high-energy electrons from northern hemispheric DMC [see yellow asterisk in Fig. 1(a) of the expected location of the DMC for the prevailing IMF orientation during MMW observations[7,9]]. Furthermore, unambiguously verifying the possible DMC source of the energetic electrons observed during microinjections would require simultaneous observations both inside and outside of the DMC on the field lines that map into the microinjection location either in the same or opposite hemisphere.

ACKNOWLEDGMENTS

K.N., Y.L., X.M., and S.K. acknowledge the support of the NASA (Grant Nos. 80NSSC18K1381 and 80NSSC22K0304) and NSF Grant No. 2308853. We also acknowledge the use of SPEDAS software used for the analysis and for creating some of the figures in this manuscript. We acknowledge use of NASA/GSFC's Space Physics Data Facility's OMNIWeb (http://omniweb.gsfc.nasa.gov) service, Orbit Visualization Tool (https://ovt.irfu.se), and WHAMP code available at https://github.com/irfu/whamp.

AUTHOR DECLARATIONS

Conflict of Interest

The authors have no conflicts to disclose.

Author Contributions

Katariina Nykyri: Conceptualization (lead); Formal analysis (lead); Funding acquisition (lead); Investigation (lead); Methodology (lead); Project administration (lead); Resources (lead); Software (lead); Supervision (lead); Visualization (lead); Writing – original draft (lead); Writing – review & editing (lead). **Yu-Lun Liou:** Software (supporting). **Xuanye Ma:** Formal analysis (supporting); Writing – review & editing (supporting). **Shiva Kavosi:** Conceptualization (supporting); Writing – review & editing (supporting). **Jan Egedal:** Conceptualization (supporting); Formal analysis (supporting); Writing – original draft (supporting); Writing – review & editing (supporting). **Stephen A. Fuselier:** Data curation (lead); Validation (supporting); Writing – review & editing

(supporting). **Roman Garcia Gomez:** Data curation (supporting); Validation (supporting).

DATA AVAILABILITY

The data that support the findings of this study are openly available in the MMS Science DataCenter accessible at https://lasp.colorado.edu/mms/sdc/public/. The versions of the data files used are v4.18.0.cdf, v3.3.0.cdf, v4.1.0.cdf, v6.1.2.cdf, v6.0.1.cdf, v3.0.1.cdf, v2.1.0.cdf for FGM (survey mode), FPI (fast mode), HPCA (survey mode), FEEPS (survey mode), EIS (survey mode), and EDP (fast mode), respectively. Furthermore, the WHAMP input used for Figs. 4–6, data and Matlab files are made available at https://doi.org/10.6084/m9.figshare.23280413.v3.[33]

REFERENCES

[1]D. L. Turner, J. F. Fennell, J. B. Blake, S. G. Claudepierre, J. H. Clemmons, A. N. Jaynes, T. Leonard, D. N. Baker, I. J. Cohen, M. Gkioulidou, A. Y. Ukhorskiy, B. H. Mauk, C. Gabrielse, V. Angelopoulos, R. J. Strangeway, C. A. Kletzing, O. Le Contel, H. E. Spence, R. B. Torbert, J. L. Burch, and G. D. Reeves, J. Geophys. Res.: Space Phys. **122**(11), 481, https://doi.org/10.1002/2017JA024554 (2017).

[2]C. Gabrielse, V. Angelopoulos, A. Runov, and D. L. Turner, J. Geophys. Res.: Space Phys. **119**, 2512, https://doi.org/10.1002/2013JA019638 (2014).

[3]D. V. Sarafopoulos, "Dispersive and repetitive Pc5 mode microinjections in the inner magnetosphere," Geophys. Res. Lett. **29**, 26, https://doi.org/10.1029/2001GL014067 (2002).

[4]J. F. Fennell, D. L. Turner, C. L. Lemon, J. B. Blake, J. H. Clemmons, B. H. Mauk, A. N. Jaynes, I. J. Cohen, J. H. Westlake, D. N. Baker, J. V. Craft, H. E. Spence, G. D. Reeves, R. B. Torbert, J. L. Burch, B. L. Giles, W. R. Paterson, and R. J. Strangeway, Geophys. Res. Lett. **43**, 6078, https://doi.org/10.1002/2016GL069207 (2016).

[5]S. Kavosi, H. E. Spence, J. F. Fennell, D. L. Turner, H. K. Connor, and J. Raeder, J. Geophys. Res.: Space Phys. **123**, 5364, https://doi.org/10.1029/2018JA025244 (2018).

[6]K. Nykyri, A. Otto, E. Adamson, E. Kronberg, and P. Daly, J. Atmos. Sol.-Terrestrial Phys. **87**, 70 (2012).

[7]K. Nykyri, C. Chu, X. Ma, S. A. Fuselier, and R. Rice, J. Geophys. Res.: Space Phys. **124**, 197, https://doi.org/10.1029/2018JA026131 (2019).

[8]K. Nykyri, J. Johnson, E. Kronberg, D. Turner, S. Wing, I. Cohen, K. Sorathia, X. Ma, B. Burkholder, G. Reeves, and J. Fennell, Geophys. Res. Lett. **48**, e2021GL092466, https://doi.org/10.1029/2021GL092466 (2021).

[9]K. Nykyri, A. Otto, E. Adamson, E. Dougal, and J. Mumme, "Cluster observations of a cusp diamagnetic cavity: Structure, size, and dynamics," J. Geophys. Res. (Space Phys.) **116**, A03228, https://doi.org/10.1029/2010JA015897 (2011).

[10]B. L. Burkholder, K. Nykyri, and X. Ma, J. Geophys. Res.: Space Phys. **126**, e2020JA028341, https://doi.org/10.1029/2020JA028341 (2021).

[11]R. M. Thorne and C. F. Kennel, J. Geophy. Res. (1896–1977) **76**, 4446, https://doi.org/10.1029/JA076i019p04446 (1971).

[12]L. R. Lyons and R. M. Thorne, J. Geophys. Res. (1896–1977) **77**, 5608, https://doi.org/10.1029/JA077i028p05608 (1972).

[13]G. V. Khazanov and K. V. Gamayunov, "Effect of electromagnetic ion cyclotron wave normal angle distribution on relativistic electron scattering in outer radiation belt," J. Geophys. Res.: Space Phys. **112**, A10209, https://doi.org/10.1029/2007JA012282 (2007).

[14]J. L. Burch, T. E. Moore, R. B. Torbert, and B. L. Giles, Space Sci. Rev. **199**, 5 (2016).

[15]C. Pollock, T. Moore, A. Jacques, J. Burch, U. Gliese, Y. Saito, T. Omoto, L. Avanov, A. Barrie, V. Coffey, J. Dorelli, D. Gershman, B. Giles, T. Rosnack, C. Salo, S. Yokota, M. Adrian, C. Aoustin, C. Auletti, S. Aung, V. Bigio, N. Cao, M. Chandler, D. Chornay, K. Christian, G. Clark, G. Collinson, T. Corris, A. De Los Santos, R. Devlin, T. Diaz, T. Dickerson, C. Dickson, A. Diekmann, F. Diggs, C. Duncan, A. Figueroa-Vinas, C. Firman, M. Freeman, N. Galassi, K. Garcia, G. Goodhart, D. Guererro, J. Hageman, J. Hanley, E. Hemminger, M. Holland, M. Hutchins, T. James, W. Jones, S. Kreisler, J. Kujawski, V. Lavu, J. Lobell, E. LeCompte, A. Lukemire, E. MacDonald, A. Mariano, T. Mukai, K. Narayanan, Q. Nguyan, M. Onizuka, W. Paterson, S. Persyn, B. Piepgrass, F. Cheney, A. Rager, T. Raghuram, A. Ramil, L. Reichenthal, H. Rodriguez, J. Rouzaud, A. Rucker, Y. Saito, M. Samara, J.-A. Sauvaud, D. Schuster, M. Shappirio, K. Shelton, D. Sher, D. Smith, K. Smith, S. Smith, D. Steinfeld, R. Szymkiewicz, K. Tanimoto, J. Taylor, C. Tucker, K. Tull, A. Uhl, J. Vloet, P. Walpole, S. Weidner, D. White, G. Winkert, P.-S. Yeh, and M. Zeuch, Space Sci. Rev. **199**, 331 (2016).

[16]C. T. Russell, B. J. Anderson, W. Baumjohann, K. R. Bromund, D. Dearborn, D. Fischer, G. Le, H. K. Leinweber, D. Leneman, W. Magnes, J. D. Means, M. B. Moldwin, R. Nakamura, D. Pierce, F. Plaschke, K. M. Rowe, J. A. Slavin, R. J. Strangeway, R. Torbert, C. Hagen, I. Jernej, A. Valavanoglou, and I. Richter, Space Sci. Rev. **199**, 189 (2016).

[17]R. B. Torbert, C. T. Russell, W. Magnes, R. E. Ergun, P.-A. Lindqvist, O. LeContel, H. Vaith, J. Macri, S. Myers, D. Rau, J. Needell, B. King, M. Granoff, M. Chutter, I. Dors, G. Olsson, Y. V. Khotyaintsev, A. Eriksson, C. A. Kletzing, S. Bounds, B. Anderson, W. Baumjohann, M. Steller, K. Bromund, G. Le, R. Nakamura, R. J. Strangeway, H. K. Leinweber, S. Tucker, J. Westfall, D. Fischer, F. Plaschke, J. Porter, and K. Lappalainen, Space Sci. Rev. **199**, 105 (2016).

[18]D. T. Young, J. L. Burch, R. G. Gomez, A. De Los Santos, G. P. Miller, P. Wilson, N. Paschalidis, S. A. Fuselier, K. Pickens, E. Hertzberg, C. J. Pollock, J. Scherrer, P. B. Wood, E. T. Donald, D. Aaron, J. Furman, D. George, R. S. Gurnee, R. S. Hourani, A. Jacques, T. Johnson, T. Orr, K. S. Pan, S. Persyn, S. Pope, J. Roberts, M. R. Stokes, K. J. Trattner, and J. M. Webster, Space Sci. Rev. **199**, 407 (2016).

[19]J. B. Blake, B. H. Mauk, D. N. Baker, P. Carranza, J. H. Clemmons, J. Craft, W. R. Crain, A. Crew, Y. Dotan, J. F. Fennell, R. H. Friedel, L. M. Friesen, F. Fuentes, R. Galvan, C. Ibscher, A. Jaynes, N. Katz, M. Lalic, A. Y. Lin, D. M. Mabry, T. Nguyen, C. Pancratz, M. Redding, G. D. Reeves, S. Smith, H. E. Spence, and J. Westlake, Space Sci. Rev. **199**, 309 (2016).

[20]B. H. Mauk, J. B. Blake, D. N. Baker, J. H. Clemmons, G. D. Reeves, H. E. Spence, S. E. Jaskulek, C. E. Schlemm, L. E. Brown, S. A. Cooper, J. V. Craft, J. F. Fennell, R. S. Gurnee, C. M. Hammock, J. R. Hayes, P. A. Hill, G. C. Ho, J. C. Hutcheson, A. D. Jacques, S. Kerem, D. G. Mitchell, K. S. Nelson, N. P. Paschalidis, E. Rossano, M. R. Stokes, and J. H. Westlake, Space Sci. Rev. **199**, 471 (2016).

[21]P.-A. Lindqvist, G. Olsson, R. B. Torbert, B. King, M. Granoff, D. Rau, G. Needell, S. Turco, I. Dors, P. Beckman, J. Macri, C. Frost, J. Salwen, A. Eriksson, L. Åhlén, Y. V. Khotyaintsev, J. Porter, K. Lappalainen, R. E. Ergun, W. Wermeer, and S. Tucker, Space Sci. Rev. **199**, 137 (2016).

[22]R. E. Ergun, S. Tucker, J. Westfall, K. A. Goodrich, D. M. Malaspina, D. Summers, J. Wallace, M. Karlsson, J. Mack, N. Brennan, B. Pyke, P. Withnell, R. Torbert, J. Macri, D. Rau, I. Dors, J. Needell, P.-A. Lindqvist, G. Olsson, and C. M. Cully, Space Sci. Rev. **199**, 167 (2016).

[23]J. H. King and N. E. Papitashvili, "Solar wind spatial scales in and comparisons of hourly wind and ACE plasma and magnetic field data," J. Geophys. Res. (Space Phys.) **110**, A02104, http://doi.org/10.1029/2004JA010649 (2005).

[24]K. Rönnmark, "WHAMP waves in homogeneous, anisotropic, multicomponent plasmas," Technical Report No. 179 (Kiruna Geophysical Institute, 1982).

[25]T. W. Moore, K. Nykyri, and A. P. Dimmock, "Cross-scale energy transport in space plasmas," Nat. Phys. **12**, 1164–1169 (2016).

[26]K. Nykyri, X. Ma, B. Burkholder, R. Rice, J. Johnson, E.-K. Kim, P. Delamere, A. Michael, K. Sorathia, D. Lin, S. Merkin, S. Fuselier, J. Broll, O. Le Contel, D. Gershman, I. Cohen, B. Giles, R. J. Strangeway, C. T. Russell, and J. Burch, J. Geophys. Res.: Space Phys. **126**, e2019JA027698, https://doi.org/10.1029/2019JA027698 (2021).

[27]D. Summers and R. M. Thorne, J. Geophys. Res.: Space Phys. **108**, 59928269, https://doi.org/10.1029/2002JA009489 (2003).

[28]J. Egedal, M. Øieroset, W. Fox, and R. P. Lin, Phys. Rev. Lett. **94**, 025006 (2005).

[29]J. Egedal, A. Le, and W. Daughton, "A review of pressure anisotropy caused by electron trapping in collisionless plasma, and its implications for magnetic reconnection," Phys. Plasmas **20**(6), 061201 (2013).

[30]B. A. Wetherton, J. Egedal, A. Le, and W. Daughton, J. Geophys. Res.: Space Phys. **125**, e2020JA028604, https://doi.org/10.1029/2020JA028604 (2021).
[31]E. Lichko and J. Egedal, Nat. Commun. **11**, 2942 (2020).
[32]J. Egedal and E. Lichko, "The fast transit-time limit of magnetic pumping with trapped electrons," J. Plasma Phys. **87**(6), 905870610 (2021).
[33]K. Nykyri and X. Ma (2023), "Wave analysis during energetic electron microinjections: A case study," figshare. https://doi.org/10.6084/m9.figshare. 23280413.v3